

Polydispersity-Driven Printing of Conformal Solid Metal Traces on Non-Adhering Biological Surfaces

Andrew Martin, Chuanshen Du, Alana M. Pauls, Thomas Ward III, and Martin Thuo*

Metals and organics possess two very dissimilar surface energies, hence, do not naturally adhere to each other. This incompatibility is exacerbated by surface roughness yet advances in wearables and bioelectronics call for their integration. Mesoscale mechanical bonds, however, transcend the necessities of surface energy matching while taking advantage of surface texture. Herein, transient carrier fluids, particle size polydispersity, and capillary-driven autonomous size-sorting are exploited to conformally jam undercooled liquid metal particles on textured soft substrate. The well packed undercooled metal particles are then chemically activated to induce phase change, leading to a solid electrically conductive metal trace. Static and dynamic deposition of the particles is amenable to this surface-templated printing of conductive traces. This process allows for printing across surfaces with varying surface features like on the brain, on paper (asymmetric porosity), or across smooth and rough brain sections. By tuning particle size and slurry concentration, good particle packing is demonstrated on a multi-scale rough surface like a rose flower. This printing method is therefore compatible with delicate (low modulus), heat sensitive, and textured substrates hence compatible with biological tissues and organic substrates.

organic materials have diametrically opposite surface energies^[1] hence, organics do not readily adhere to metals.^[5] This paradoxical juxtaposition, however, can be overcome through scaling,^[6] self-assembly,^[7] and mechanical bonds.^[8] We infer that non-Hertzian behavior of soft granular matters^[9] combined with capillary self-assembly,^[7] self-filtration,^[7b,10] and jamming^[10b,11] can lead to conformal mechanical bonds across dissimilar materials. Where the granular matters are undercooled liquid metal particles, sintering and solidification enable heat-free fabrication of conformal physisorbed (removable) conductive traces on virtually any textured or low modulus surface.^[12]

Deposition of solvent-suspended polydisperse metal particles onto textured surfaces forms a self-sorted tightly packed sediment through solvent evaporation-driven capillary self-assembly^[7b] combined with self-filtration.^[10b] Self-filtration is the process by which relatively large particles will clog

1. Introduction

Advances in wearable, flexible, and printed electronics, inevitably calls for integration of electronics onto organic substrates and tissue. A major caveat is ability to interface these rather dissimilar outfits due to mismatch in modulus, surface energy,^[1] reactivity,^[2] conductivity,^[3] processing temperature,^[4] among other properties. Inorganic (e.g., metals) and

or “jam” when passing through pores/fissures (Figure 1a).^[10b] Solvent evaporation begins at the gas–liquid interface then penetrates through the self-filtered larger particles (Figure S1 and discussion in the Supporting Information). For soft deformable particles the drying process induces capillary-driven packing resulting in higher densification than in non-deformable analogues.^[13] This process leads to reversible convergence of the particle ensemble stress field (Figure S1c, Supporting Information). Solvent evaporation also generates a capillary pressure gradient allowing smaller particles to pass through gaps formed by jammed larger ones (Figure S1a,b, Supporting Information).^[10a] For the phenomena to occur, particle size polydispersity (large-to-small particle diameter) needs to be on the order of 1:3–7 (Figure S1, Supporting Information).^[7b,10b,14] With decreasing dimensions, or over multi-scale pore dimensions, this process repeats ad infinitum leading to an autonomous size-differentiated packing of polydisperse slurries. Capillary self-assembly combined with self-filtration ensures that these particles are immobilized (jammed), creating a multi-layer self-locking particle bed (Figure 1a,b).^[7,10b,14] The amount of self-filtration can be approximated through a pressure-dependent relationship (Equation (1), details in the Supporting Information)^[10a]

$$\phi_{\text{out}} = \frac{\phi_{\text{in}}}{1 + A \frac{\Pi_2}{\rho g H_1} (1 - \phi_{\text{in}})} \quad (1)$$

A. Martin, C. Du, A. M. Pauls, Prof. M. Thuo
Department of Materials Science and Engineering
Iowa State University
Ames, IA 50011, USA
E-mail: mthuo@iastate.edu

Prof. T. Ward III
Department of Aerospace Engineering
Iowa State University
Ames, IA 50011, USA

Prof. M. Thuo
Micro-Electronics Research Centre
Ames, IA 50011, USA

Prof. M. Thuo
Department of Electrical and Computer Engineering
Iowa State University
Ames, IA 50011, USA

 The ORCID identification number(s) for the author(s) of this article can be found under <https://doi.org/10.1002/admi.202001294>.

DOI: 10.1002/admi.202001294

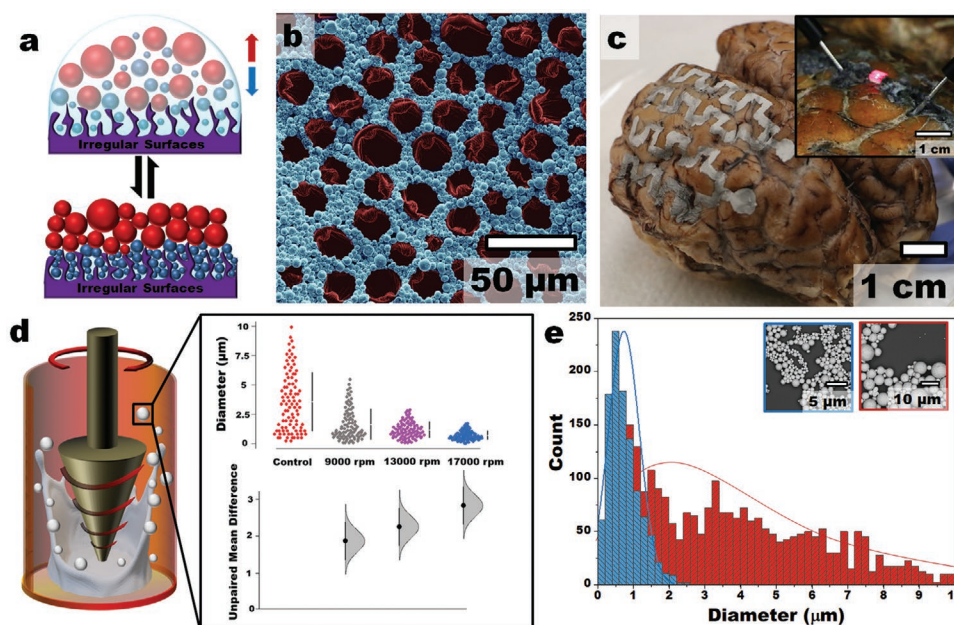


Figure 1. Design of the universal printing method across varied surfaces. a) Schematic of particle self-filtration and jamming on irregular surfaces. b) SEM image of particles printed on a rose petal illustrating templating. c) Cow brain with printed circuits (inset: activated LED soldered on the brain surface). d) Schematic of the SLICE process with estimation plots that reveal magnitude of the effect of shearing speed. e) Histograms and associated Gaussian fits of particle size distribution from different synthesis condition (red: low shear speed and blue: high shear speed).

where ϕ_{out} is the outlet fraction of the self-filtering particle in solution, ϕ_{in} is the inlet fraction, A is a dimensionless value based on the spatial dependence in shear rate experienced by the particles (typically 0.34 ± 0.04),^[10a] Π is particle pressure (compressive stress exerted by the particles under suspension), ρ is density, g is gravitational acceleration, and H is height of the solvent. This equation predicts the amount of self-filtration by smaller particles between gaps formed by larger particles (Figure S1a,b, Supporting Information) and further into the channels of textured surfaces. With further solvent evaporation, larger particles ultimately clog and get locked in place while smaller particles percolate through created gaps (Figure S1c, Supporting Information). The propensity to jam is related to the ratio of channel dimension to particle radius.^[12a] This jammed state ensures that deposited materials are mechanically stabilized and, therefore, can be sintered into surface-templated conformal networks (Figure 1b,c). We infer, and demonstrate, that appropriately tuned particle polydispersity (Figure 1d,e; Figures S1–S4, Supporting Information) abets self-filtration and jamming on a wide-range of textured surfaces. In a multi-scale textured surface however, the wider the polydispersity the higher the likelihood of packing into all available fissures. Felicitous choice of processing conditions, backed by empirical statistical inferences in the shearing liquids into complex particles (SLICE)^[15] method, reliably gives desired particle polydispersity (Figure 1d). It is, therefore, feasible that on multi-scale textured surfaces, polydisperse undercooled liquid metal core-shell (ULMCS) particles can be tuned to enable autonomous size-driven percolative sorting and jamming leading to surface-templated printing of conductive metallic traces on surface energy mismatched surfaces. We demonstrate this concept over a range of biological substrates bearing varied surface asperities.

While other types of conductive inks such as liquid metals (e.g., EGaln) and silver inks have reported printability of biological substrates, mechanisms that drive adhesion to textured biological substrates were not elaborated.^[16] The key differences and advantages of the currently reported method over the liquid metals and silver inks include: i) We demonstrate a conformal mechanical bond with a textured substrate (physisorption)^[17] enabled by autonomous self-filtration, high densification, and jamming. Whereas the same can be achieved with other liquid metal particles, the bond is further stabilized through heat-free sintering to create a solid contact—a feat that cannot be achieved with ambient liquid metals or the silver inks. The sintering process induces solidification rendering printed lines to maintain their form factor while also being weakly bonded to the substrate which enables ease of removal.^[15b] Ambient liquid metals like EGaln lines whilst having the advantages of deformability and stretchability^[16a,d,18] (due to liquid state) do not sinter and solidify to maintain its form-factor. For textured surfaces, fracture of the oxide shell of ambient liquid metals leads to deposition of the metal in crevasses where it is difficult to remove due to capillary pressure. ii) The reported process does not rely on specific viscous carrier fluid or a certain viscosity to print. Flexibility in the carrier fluid implies that the resolution of the printed lines is largely dictated by particle size distribution (nm to μm scale). Silver inks (flakes or nanoparticles) rely on viscous carrier medium, hence the structural packing that can be attained on a multi-scale surface is dependent on the capillary length of the carrier fluid (mm to cm scale).^[16b,19] Furthermore, sintering of these silver inks often requires heat, a variable that is incompatible with most soft delicate substrates.^[15b]

We infer that soft (deformable) ULMCS particles would show relatively higher packing ratio ($\Phi \approx 0.6\text{--}0.7$)^[9b] and stress-driven

densification compared to solid spheres.^[20] This densification is further abetted by attractive capillary forces, F_b , especially on reaching the pendular state in solvent-assisted deposition.^[9a,21] Equation (2) shows that favorable wetting by carrier fluid enhances F_b hence higher densification.

$$F_b = 2\pi b\gamma \cos\theta \quad (2)$$

where b is approximately 10% of particle radius,^[14a] γ is surface tension, and θ is the Young–Dupré equation derived contact angle.^[5a] With large particle size polydispersity, in a wetting carrier fluid, F_b (Equation [2]) and Π (Equation [1]) imply self-filtration and jamming. Incorporation of a kinetically-frustrated chemical trigger in the carrier fluid to induce heat-free sintering and phase change (so-called coalescence of undercooled particles through chemical trigger—CUPACT^[15b]), results in solidification of the metal particles in their most conformal configuration. This delayed heat-free solidification of metals guarantees minimum perturbation of the underlying features and that the formed traces conform to surface features albeit limited by smallest particle size. The resulting porous network of metallic interconnects (particles joined only via loci of the capillary bridge), allows efficient fluid diffusion while offering stable conductive traces even on surface energy mismatched substrates. Herein, we validate this ansatz by: i) Demonstrating a predictive approach to tuning particle size-polydispersity (Figure 1d,e), ii) surface-feature templated deposition of ULMCS particles on surface-energy mismatched substrates—such as rose petals (Figure 1b) and brain (Figure 1c). iii) Sintering the assembled particles to create electrically conductive traces, and, iv) exploiting fluid–solid duality of granular matter in a jamming–unjamming (convergence and divergence of stresses, respectively) process (Figure S1, Supporting Information)^[22] to render fabricated traces recoverable via solvent-assisted shearing (akin to Reynolds dilation of wet sand).^[23]

1.1. Tunable Polydispersity

Packing and densification of granular matter strongly relates to particle size polydispersity and is enhanced by a positive skew in size distribution.^[24] To develop a generalized approach to tuning particle polydispersity, undercooled Field's metal (Bi: 32.5, In: 51, Sn: 16.5 wt%, $T_m = 62^\circ\text{C}$) particles were synthesized via the SLICE method^[15c] at various shear times and shear speeds (Figures S2–S4, Supporting Information). To quantitatively delineate effect of processing conditions (time or shear) on size and degree of undercooling, we deployed statistics (probability plots, confidence bands, and estimation plots) tools to generate simplified design rules.

To deduce effect of shear time, samples were sheared at 13 000 rpm for 5–30 min. Similarly, to evaluate the effect of shear stress, all samples were prepared over 10 min but at 6000–17 000 rpm. By keeping the shear tool, quantities of both processed metal and shearing liquid constant, rotor speed could be correlated to shear stress. **Figure 2a** shows trends in average particle size with change in shear time and shear speed (akin to stress). A general decrease in particle size is observed albeit with a larger response to speed than time. Reduction in

particle size correlated with convergence in their size distribution (Figure 2a,b). To quantify the magnitude of shear stress or shear time on average particle size, hence ascertain the most important parameter in engineering polydispersity, we utilized estimation plots (Figure 2b). We observe that the unpaired mean difference is 5× higher for shear speed than for shear time. This affirms that, in the SLICE method, work done on the particle is significantly more important^[27] than any ensuing surface chemistry or equilibration. The unpaired mean for shear time rapidly asymptotes confirming that time is a limited parameter in tuning size distribution. Shear stress, however, shows a rapid increase over the entire evaluated range. By normalizing particle sizes distributions, polydispersity probability plots (Figure 2c; Figure S5, Supporting Information) are generated as guides to likelihood of attaining a desired size range.

1.2. Effect of Polydispersity on Undercooling

Adopted synthesis conditions, however, should have no adverse effects on degree of undercooling ($\Delta T/T_m$) for the ansatz to be realized. Degree of undercooled is inversely correlated to particle size,^[25] hence, shear stress shows a rapid increase in $\Delta T/T_m$ than shear time (Figure 2d). For ambient fabrication of Field's metal interconnected networks, a minimum $\Delta T/T_m \approx 0.11$ is needed, hence an upper limit of $\approx 5\ \mu\text{m}$ in the engineered dispersion. This prediction implies that particles need to be prepared at a shear rate $\geq 9000\ \text{rpm}$ (Figures S2,S3, Supporting Information).

1.3. Universal Printing

Having established parameters to prepare polydisperse metal particle without loss of undercooling, we demonstrate use of capillary adhesion, self-filtration, and jamming to create physisorbed conductive traces between metals and an array of textured surfaces. First, we explored fit to multi-scale roughness on a rose petal given that bumps on a rose petal are $<8.5\ \mu\text{m}$ in height with a large slant (peak-width:mid-width ratio = 1:3).^[1a,26] This texture implies that for diameter $\approx 4.5\ \mu\text{m}$, only a single particle can fit into the grooves, hence self-filtration occurs with the smallest particles settling at the bottom of the crevices (see Figure S1, Supporting Information). **Figure 3a** shows as-deposited particles (drop cast using 9000 rpm sample) on a rose petal, and as expected, larger particles are mostly trapped on top. The particles organize into hexagonal patterns across the petal surface templating the inter-bump space (Figure 1a,b).

Chemical sintering through CUPACT (Figure 3a) or applying shear stress in the dry state (Video S1 and Figure S6a,b, Supporting Information) does not perturb these patterns indicating that they are jammed in place. Depositing particles under shear stress (spin coating) or by drop casting gives analogous structures (Figure S6c–f, Supporting Information) suggesting that this method of printing is amenable to static (drop casting) and dynamic (spin coating) process. To capture the importance of capillary forces (self-filtration and jamming), we fabricated similar autonomous size-sorting structures on Whatman chromatography paper #1—a porous, tortuous, multi-scale textured

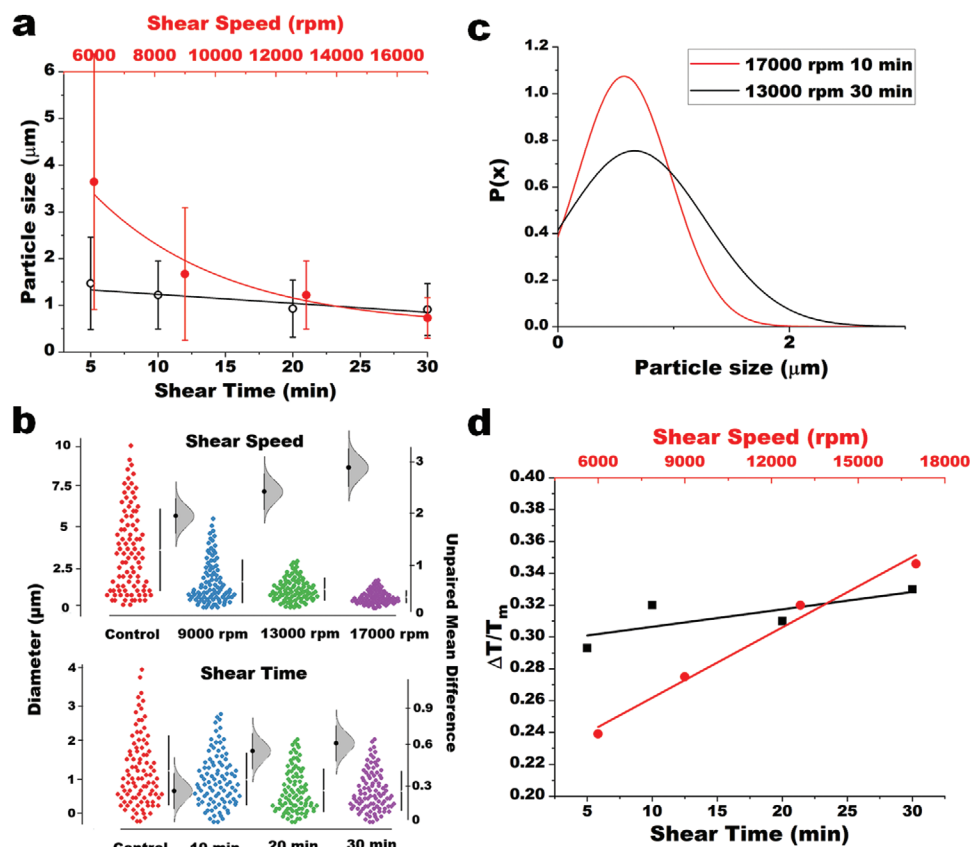


Figure 2. Statistical analysis of particle size polydispersity and undercooling of synthesized particles. a) Dependence of particle size on synthesis condition, the lines are guides for the eye and are not meant to be fit to the data. b) Differentiating magnitude of the effect of shear speed (stress) and shear time using estimation plots. c) Representative Gaussian fits for evaluated maximum time and shear speed. d) Effect of synthesis conditions on degree of undercooling.

material, using polydisperse particles synthesized at 6000 rpm that have a large (up to 10 μm) size distribution (Figure S2, Supporting Information). Template-stripped inverted pattern from a rose (Figure 3b) as well as a cross-section image of the paper with deposited particles (Figure 3c) confirm self-filtration, with inner layer (false colored blue) filling with predominantly smaller particles while the outer layer (false colored red) is dominated by larger particles.^[27] Interestingly, the particles do not traverse the thickness of the paper which we infer to be due to F_b (Equation [2]). This observation implies that not only can the slurry of these polydisperse particles self-filter, but the capillary forces of the carrier fluid can be exploited to dictate percolation into a porous network. This is of critical importance while depositing these metallic traces across surface with varying degrees of porosity and where only surface contact and complete particle networks are desired (e.g., interior of the brain, Figure 3d).

To ascertain the utility and versatility of this method, we explored printing conductive traces on soft membranes and tissue. Due to the abundance of these fusible alloy elements (e.g., Bi, In, and Sn) in nature, the biocompatibility of said elements has been previously extensively researched.^[28] We fabricated traces on various cow tissues like brain (Figure 3d,e; Figure S7a,b, Supporting Information) and heart (Figure 3f); followed by heat-free metal solidification and sintering via

CUPACT to render the particles conductive (Figure 3g–j) without damaging the tissue. Figure S7a,b, Supporting Information, shows printing of electrically conductive lines on surface connective tissue (Video S2, Supporting Information) without permeation into the brain. Due to the small particle interconnection bridges, films derived from CUPACT are more resistive than the bulk metal (63 $\mu\Omega\text{-cm}$ vs 52 $\mu\Omega\text{-cm}$) depending on the activating chemical stimuli.^[15b] These lines are, therefore, expected to be electrically conductive, albeit, with slightly increased resistive heating than the bulk metal.

To illustrate this conjecture, we printed conductive traces inside the brain across different surface textures (Figure 3d,e; Figure S7c,d, Supporting Information). Besides glial and neuronal cells, majority of the brain is lipophilic (almost 60% fat)^[29] hence not amicable to bonding with metals due to surface energy mismatch and/or mismatch in tolerance to heat. Differences in density ($\approx 1 \text{ g cm}^{-3}$ vs 7 g cm^{-3}), however, allows for precipitation-induced texturing as the metal particles settle on the surface of the low modulus tissue. For clarity, Figure S9, Supporting Information, shows indents that can be created on a thin smooth polymer film via soft impingement with polydisperse liquid metal particles. Transition from a fat-rich region to a networked porous region enables capillary-limited deposition over the pores (Figure 3d) akin to that observed above with paper (Figure 3c). This

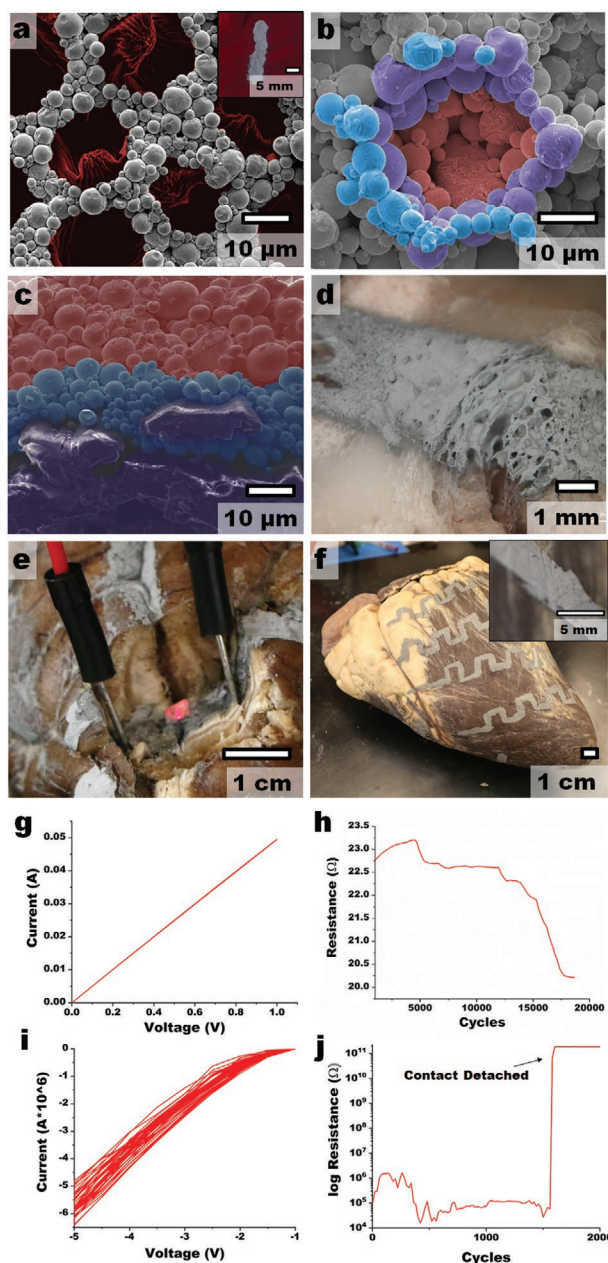


Figure 3. Universal metal printing on various surfaces. a) SEM image of rose petal (false colored red) surface-templated metal particles after sintering through CUPACT. b) Template stripped patterns of particles sintered on rose petal displaying self-filtration and c) SEM image of a cross-section of a line printed on paper with small particles false colored blue and larger particles red for clarity. d) Line printed on the surface of brain's interior across a fatty flat region and a porous interlayer. e) Metallic traces on the interior of the brain showing conductivity as soldered LED glows. f) Metal printing on a cow heart, inset shows a close-up of the printed lines. g) 200 cycles I - V curve and h) resistance change over 20 000 cycles on conductive line printed on paper. i) 200 cycles I - V curve on conductive line printed on brain. j) Resistance change overtime for repeated voltage cycle for conductive line printed on brain.

precipitation-induced texturing also allows these conductive traces to indent and adhere to connective tissues (Figure S7a,b, Supporting Information) implying that a conductive line can

be deposited via screen printing across a varying set of surface roughness on a tissue.

Besides brain, electrical connectivity to the heart—though vital in cardiac intervention, is challenging in part due to the pericardium. The complexity in structure, modulus, and function, coupled with surface energy mismatch of the protective pericardium sac to metals renders fabrication of conductive networks on the heart surface challenging. Underlying pericardial fluid and flexibility of the surface of the heart, however, implies that deposition of the denser metallic particles would lead to induced texturing hence mechanical bonding. Figure 3f shows conductive metallic traces fabricated on a heart where the lines form over fat and muscle tissue akin to the brain. Previous studies of films derived from CUPACT^[15b] inspires us to infer that though these traces are formed on fixed tissue, similar functional structures can be made on living analogues.

To ascertain that the metal particles are sintered, connected, and conductive, repeated voltage cycles were applied to the printed lines. For brevity, we evaluated printed lines on paper and brain (Video S5, Supporting Information) and infer prior work^[15b] on free standing CUPACT films. On a stable organic structure (paper), the printed lines are conductive and stable for $\approx 10\,000$ sweeps (between ≈ 5000 and $15\,000$ cycles) as no significant change in I - V characteristics is observed (Figure 3g,h). When cycled over longer times however, as expected, a slight drift in conductivity (hence resistance) is observed (Figure 3h). Resistivity of, $\rho = 14.9 \pm 0.5\text{ m}\Omega\text{-cm}$ was observed under the current activation conditions over the course of 20 000 voltage cycling (Figure 3g,h). This number is higher compared to previous results^[15b] due to inter-particle capillary entrapment of the viscous carrier medium used in the ink. The formation of a non-conductive organic adlayer between the particle necks increasing overall resistivity (Figure S8c-e, Supporting Information). To lower the resistivity, volatile lower viscosity carrier fluids may be used to give films with resistivity $\approx 60\text{ }\mu\Omega\text{-cm}$, as previously reported,^[15b] albeit with challenges in biocompatibility. On an uneven, malleable, heat-sensitive biological tissue, however, the line shows a decaying trend over the repeated cycles (Figure 3i). Lines printed on brain are conductive for >1000 cycles albeit with higher resistivity. We observed that this higher resistivity of traces on the brain lead to loss of contact (detachment) likely due to joule heating, this effect results on extreme deformation of the detached tissue (Figure 3j; Figure S8c, Supporting Information). This process, however, seems unlikely in a well hydrated tissue. The higher resistivity seen in the brain tissue compared to the paper is expected due to the non-uniformity and irregularity of the substrate and likely network contamination from occluded bio-adducts during the precipitation and CUPACT processes.

Finally, since the conductive traces on soft tissue are mechanically physisorbed networks (via jamming and small interparticle necks, Figure S7e,f, Supporting Information) mechanical breakage of the connecting necks can be achieved without significant amount of work. Shear driven fracture of these necks in presence of a Newtonian fluid renders interparticle stress divergent.^[22a,b] Fracture of the necks re-introduces flow and particle displacement under a small shear load (Figures S1c,S8a,b, and Video S3, Supporting Information). This implies that the reported method is a heat-free mechanical-bonding driven

reversible printing of metallic conductive traces on rather complex soft or textured substrates. A key advantage of this approach is the insensitivity to biological fluids since metals do not swell under aqueous media.

2. Conclusions

Herein, we illustrate the versatility of mechanical bonding on surface energy mismatched surfaces via a self-filtration, capillary assembly, jamming, and heat-free sintering across non-Hertzian contacts to print conductive metallic traces—without damaging sensitive tissue or underlying substrate surface asperities. The bedrock of this method is ability to predictively tune particle size polydispersity to match complexity of the substrate surface without compromising degree of undercooling. By adopting appropriate probabilistic predictive tools, appropriate processing conditions can be determined apriori to enable synthesis of desired particle sizes for maximal self-filtration and jamming. We exploit differences in density to induce texture on smooth soft surfaces, hence bonding. Besides deposition of metallic traces, tuning particle size polydispersity to match surface features can enable unprecedented templated patterning with delicate bio-surfaces like the rose flower or creation of stochastic surface texture on soft, thin films.

3. Experimental Section

Materials: Field's metal (eutectic indium, 51%-bismuth, 32.5%-tin, 16.5%) was purchased from Rotometals Inc. Glacial acetic acid (99.7%), ethyl acetate (99.9%) were from Fisher Scientific. Diethylene glycol (99.9%) was purchased from VWR. 2-Hydroxyethyl cellulose ($\approx 720\,000\text{ M}_w$) was purchased from Aldrich Chemistry. Preserved cow brain and cow heart were purchased from Bio Corporation, the samples were stored in a refrigerator and thawed before use. All commercially available preserved samples do not require an IRB approval, and were disposed following approved procedures as advised by Iowa State University environmental health services.

Undercooled Particles Synthesis: Undercooled metal particles made from Field's metal were synthesized following the SLICE method.^[15c] Detailed procedure is provided in the Supporting Information.

Preparation of Field's Metal Ink for Direct Printing: Methanol and water were mixed in a 1:1 solution to form the carrier fluid. Hydroxyethyl cellulose (2%, 0.02 g mL⁻¹) was dissolved in the carrier fluid while stirring at 70 °C. The solution was then cooled to room temperature. A 75 wt% metal ink was then created by adding the cellulose solution into dried ULMCS particles. The dispersion was homogenized using a vortex mixer (Fisher brand). Deposition of the slurry was done either with a paint brush onto a screen made from painter's tape or using direct deposition using pipet.

Chemical Sintering: CUPACT method was previously published.^[15b] Printed particles were dried out on desired substrates. Chemical fluxes were made using 60% v/v acetic acid diluted in ethanol and a drop of water. This flux was then applied on the particle film followed by drying under ambient conditions to sinter the particle bed.

Estimation Plots: The estimation plots were generated using the estimation statistics beta code (www.estimationstats.com).

Supporting Information

Supporting Information is available from the Wiley Online Library or from the author.

Acknowledgements

The authors would like to thank Tracey Stewart for the help with stereo light microscopy on the brain cross-section. This work was supported by Iowa State University through Intellectual Property Royalty and a Black & Veatch faculty fellowship.

Conflict of Interest

The authors declare no conflict of interest.

Keywords

bio-compatible, electronics, mechanical bonding, soft tissue, universal printing

Received: July 22, 2020

Revised: August 19, 2020

Published online: September 9, 2020

- [1] a) B. Bhushan, M. Nosonovsky, *Philos. Trans. R. Soc., A* **2010**, 368, 4713; b) T. V. Stirbat, A. Mgharbel, S. Bodennec, K. Ferri, H. C. Mertani, J.-P. Rieu, H. Delanoë-Ayari, *PLoS One* **2013**, 8, e52554; c) R. Shuttleworth, *Proc. Phys. Soc., London, Sect. A* **1950**, 63, 444.
- [2] J. A. Gardella, N. L. Hernandez de Gatica, *J. Electron Spectrosc.* **1996**, 81, 227.
- [3] M. J. Peters, J. G. Stinstra, I. Leveles, *Modeling and Imaging of Bioelectrical Activity: Principles and Applications* (Ed: B. He), Springer US, Boston, MA **2005**, p. 281.
- [4] X. He, *Open Biomed. Eng. J.* **2011**, 5, 47.
- [5] a) J. N. Israelachvili, *Intermolecular and Surface Forces*, Academic Press, Cambridge **2011**; b) Q. Jiang, Z. Wen, *Thermodynamics of Materials*, Springer, Berlin **2011**.
- [6] a) K. Kroy, *Biophys. J.* **2016**, 111, 898; b) Z. Zhang, X. Ge, Y. Li, *Acta Mech. Solida Sin.* **2006**, 19, 196; c) A. Gautieri, M. J. Buehler, *Mateomics: Multiscale Mechanics of Biological Materials and Structures* (Eds: M. J. Buehler, R. Ballarini), Springer, Vienna **2013**, p. 13.
- [7] a) L. Malaquin, T. Kraus, H. Schmid, E. Delamarche, H. Wolf, *Langmuir* **2007**, 23, 11513; b) N. R. Morrow, *Ind. Eng. Chem.* **1970**, 62, 32.
- [8] C. J. Bruns, J. F. Stoddart, *The Nature of the Mechanical Bond* (Eds: C. J. Bruns, J. F. Stoddart), John Wiley & Sons, New Jersey **2016**.
- [9] a) S. Herminghaus, *Adv. Phys.* **2005**, 54, 221; b) S. H. E. Rahbari, M. Khadem-Maaref, S. K. A. Seyed Yaghoubi, *Phys. Rev. E* **2013**, 88, 042203.
- [10] a) S. D. Kulkarni, B. Metzger, J. F. Morris, *Phys. Rev. E* **2010**, 82, 010402; b) M. D. Haw, *Phys. Rev. Lett.* **2004**, 92, 185506.
- [11] a) R. P. Behringer, *C. R. Phys.* **2015**, 16, 10; b) R. Lespiat, S. Cohen-Addad, R. Höhrer, *Phys. Rev. Lett.* **2011**, 106, 148302.
- [12] a) S. Yang, J. R. G. Evans, *Powder Technol.* **2004**, 139, 55; b) S. Zhang, L. Zhang, M. Bouzid, D. Z. Rocklin, E. Del Gado, X. Mao, *Phys. Rev. Lett.* **2019**, 123, 058001.
- [13] J. Mattsson, H. M. Wyss, A. Fernandez-Nieves, K. Miyazaki, Z. Hu, D. R. Reichman, D. A. Weitz, *Nature* **2009**, 462, 83.
- [14] a) L. Xu, S. Davies, A. B. Schofield, D. A. Weitz, *Phys. Rev. Lett.* **2008**, 101, 094502; b) A. S. Dimitrov, K. Nagayama, *Langmuir* **1996**, 12, 1303.
- [15] a) S. Çınar, I. D. Tevis, J. Chen, M. Thuo, *Sci. Rep.* **2016**, 6, 21864; b) A. Martin, B. S. Chang, Z. Martin, D. Paramanik, C. Frankiewicz, S. Kundu, I. D. Tevis, M. Thuo, *Adv. Funct. Mater.* **2019**, 29, 1970278; c) I. D. Tevis, L. B. Newcomb, M. Thuo, *Langmuir* **2014**, 30, 14308.

- [16] a) M. Tavakoli, M. H. Malakooti, H. Paisana, Y. Ohm, D. G. Marques, P. A. Lopes, A. P. Piedade, A. T. de Almeida, C. Majidi, *Adv. Mater.* **2018**, *30*, 1801852; b) N. X. Williams, S. Noyce, J. A. Cardenas, M. Catenacci, B. J. Wiley, A. D. Franklin, *Nanoscale* **2019**, *11*, 14294; c) Z. Zhu, S. -Z. Guo, T. Hirdler, C. Eide, X. Fan, J. Tolar, M. C. McAlpine, *Adv. Mater.* **2018**, *30*, 1707495; d) R. Guo, B. Cui, X. Zhao, M. Duan, X. Sun, R. Zhao, L. Sheng, J. Liu, J. Lu, *Mater. Horiz.* **2020**, *7*, 1845; e) F. Ershad, A. Thukral, J. Yue, P. Comeaux, Y. Lu, H. Shim, K. Sim, N. -I. Kim, Z. Rao, R. Guevara, L. Contreras, F. Pan, Y. Zhang, Y. -S. Guan, P. Yang, X. Wang, P. Wang, X. Wu, C. Yu, *Nat. Commun.* **2020**, *11*, 3823.
- [17] A. Zangwill, *Physics at Surfaces*, Cambridge University Press, Cambridge **1988**.
- [18] a) M. D. Dickey, *Adv. Mater.* **2017**, *29*, 1606425; b) M. D. Dickey, R. C. Chiechi, R. J. Larsen, E. A. Weiss, D. A. Weitz, G. M. Whitesides, *Adv. Funct. Mater.* **2008**, *18*, 1097.
- [19] A. Russo, B. Y. Ahn, J. J. Adams, E. B. Duoss, J. T. Bernhard, J. A. Lewis, *Adv. Mater.* **2011**, *23*, 3426.
- [20] a) R. K. Bordia, G. W. Scherer, *Acta Metall.* **1988**, *36*, 2393; b) G. W. Scherer, T. Garino, *J. Am. Ceram. Soc.* **1985**, *68*, 216; c) A. Jagota, C. Y. Hui, *Mech. Mater.* **1990**, *9*, 107; d) A. H. Clark, L. Kondic, R. P. Behringer, *Phys. Rev. Lett.* **2012**, *109*, 238302; e) A. H. Clark, A. J. Petersen, L. Kondic, R. P. Behringer, *Phys. Rev. Lett.* **2015**, *114*, 144502.
- [21] a) D. J. Hornbaker, R. Albert, I. Albert, A. L. Barabási, P. Schiffer, *Nature* **1997**, *387*, 765; b) N. Mitarai, F. Nori, *Adv. Phys.* **2006**, *55*; c) S. Nowak, A. Samadani, A. Kudrolli, *Nat. Phys.* **2005**, *1*, 50; d) M. Scheel, R. Seemann, M. Brinkmann, M. D. i Michiel, A. Sheppard, B. Breidenbach, S. Herminghaus, *Nat. Mater.* **2008**, *7*, 189.
- [22] a) V. Trappe, V. Prasad, L. Cipelletti, P. N. Segre, D. A. Weitz, *Nature* **2001**, *411*, 772; b) A. J. Liu, S. R. Nagel, *Jamming and Rheology : Constrained Dynamics on Microscopic and Macroscopic Scales*, Taylor & Francis, London **2001**; c) R. G. Larson, *The Structure and Rheology of Complex Fluids*, Oxford University Press, New York **1999**.
- [23] O. Reynolds, *Philos. Mag.* **1885**, *20*, 469.
- [24] K. W. Desmond, E. R. Weeks, *Phys. Rev. E* **2014**, *90*, 022204.
- [25] B. Vonnegut, *J. Colloid Sci.* **1948**, *3*, 563.
- [26] a) B. Bhushan, E. K. Her, *Langmuir* **2010**, *26*, 8207; b) B. Bhushan, M. Nosonovsky, in *Encyclopedia of Nanotechnology* (Ed: B. Bhushan), Springer, Netherlands, Dordrecht **2012**, p. 2265.
- [27] J. J. Chang, A. Martin, C. Du, A. Pauls, M. M. Thuo, *Angew. Chem., Int. Ed.* **2020**, <https://doi.org/10.1002/anie.202008621>.
- [28] a) M. Nakajima, M. Usami, K. Nakazawa, K. Arishima, M. Yamamoto, *Congenital Anomalies* **2008**, *48*, 145; b) L. Yi, J. Liu, *Int. Mater. Rev.* **2017**, *62*, 415; c) H. Rüdell, *Ecotoxicol. Environ. Saf.* **2003**, *56*, 180; d) R. Mohan, *Nat. Chem.* **2010**, *2*, 336.
- [29] a) C. Y. Chang, D. S. Ke, J. Y. Chen, *Acta Neurol.* **2009**, *18*, 231; b) B. Mota, S. Herculano-Houzel, *Front. Neuroanat.* **2014**, *8*, 127.